RNA–protein binding interface in the telomerase ribonucleoprotein

Christopher J. Bley[a], Xiaodong Qi[a], Dustin P. Rand[a], Chad R. Borges[b], Randall W. Nelson[b], and Julian J.-L. Chen[a,1]

[a]Department of Chemistry and Biochemistry, and [b]Biodesign Institute, Arizona State University, Tempe, AZ 85287

Edited by Neal F. Lue, Weill Cornell Medical College, New York, NY, and accepted by the Editorial Board November 8, 2011 (received for review July 29, 2011)

Telomerase is a specialized reverse transcriptase containing an intrinsic telomerase RNA (TR) which provides the template for telomeric DNA synthesis. Distinct from conventional reverse transcriptases, telomerase has evolved a unique TR-binding domain (TRBD) in the catalytic telomerase reverse transcriptase (TERT) protein, integral for ribonucleoprotein assembly. Two structural elements in the vertebrate TR, the pseudoknot and CR4/5, bind TERT independently and are essential for telomerase enzymatic activity. However, the details of the TR–TERT interaction have remained elusive. In this study, we employed a photoaffinity cross-linking approach to map the CR4/5-TRBD RNA–protein binding interface by identifying RNA and protein residues in close proximity. Photoreactive 5-iodouridines were incorporated into the medaka CR4/5 RNA fragment and UV cross-linked to the medaka TRBD protein fragment. The cross-linking RNA residues were identified by alkaline partial hydrolysis and cross-linked protein residues were identified by mass spectrometry. Three CR4/5 RNA residues (U182, U187, and U205) were found cross-linking to TRBD amino acids Tyr503, Phe355, and Trp477, respectively. This CR4/5 binding pocket is distinct and separate from the previously proposed T pocket in the *Tetrahymena* TRBD. Based on homologous structural models, our cross-linking data position the essential loop L6.1 adjacent to the TERT C-terminal extension domain. We thus propose that stem-loop 6.1 facilitates proper TERT folding by interacting with both TRBD and C-terminal extension. Revealing the telomerase CR4/5-TRBD binding interface with single-residue resolution provides important insights into telomerase ribonucleoprotein architecture and the function of the essential CR4/5 domain.

Telomerase maintains telomere length through de novo synthesis of telomeric DNA repeats onto chromosome ends. Telomeres function to distinguish native chromosome ends from double-strand breaks (1). Cells lacking active telomerase exhibit progressive telomere shortening and reduced replicative capacity. Mutations in telomerase genes cause telomerase deficiency, leading to telomere attrition and a number of human diseases including dyskeratosis congenita, aplastic anemia, and idiopathic pulmonary fibrosis (2). Furthermore, telomerase is activated in the vast majority of cancer cells, bypassing senescence induced by critically short telomeres (3). Understanding the mechanism and architecture of telomerase is thus essential for the development of therapies for telomere-mediated diseases.

Unlike conventional reverse transcriptase (RT), telomerase functions as a ribonucleoprotein (RNP) containing a catalytic telomerase reverse transcriptase (TERT) and the telomerase RNA (TR) (4). TERT comprises four major structural domains: the telomerase essential N terminus (TEN) domain, the telomerase RNA-binding domain (TRBD), the RT domain, and the C-terminal extension (CTE) domain. In addition to providing the template for DNA synthesis, the TR contains two highly conserved structural domains: the template-proximal pseudoknot structure that forms a triple helix and the three-way helical junction, referred as the CR4/5 domain in vertebrates (5–7). The pseudoknot and CR4/5 domains are essential for telomerase activity and bind independently to two distinct TERT domains, TEN and TRBD, respectively (8–10).

The TRBD primary sequence from all known species contains three highly conserved motifs: CP, QFP and T (11, 12). The vertebrate TRBD contains an additional vertebrate-specific RNA binding (VSR) motif (9). Substitution and deletion studies found CP, QFP, T, and VSR motifs are required for CR4/5 binding in vertebrates (9, 13, 14). In budding yeast, the TR contains a conserved three-way junction structure that is similar to the vertebrate CR4/5 domain but does not appear to bind TRBD in vitro (15). The ciliate TR lacks a three-way junction but contains the conserved stem-loop IV that binds TRBD and might function analogously to the vertebrate CR4/5 domain (16–21). Although the structures of TRBD from *Tetrahymena thermophila* and *Tribolium castaneum* (red flour beetle) have been determined by X-ray crystallography (22, 23), the details of the TR-TRBD binding interface remain elusive.

In this study, we map the binding interface between the TR-CR4/5 domain and the TERT-TRBD from the teleost fish *Oryzias latipes* (Japanese medaka). Medaka has the smallest known vertebrate TR of only 312 nt and a highly compact CR4/5 structure (24). Through 5-iodouridine (5IU) mediated cross-linking, the in vitro transcribed CR4/5 RNA fragment can efficiently and specifically cross-link to recombinant medaka TRBD protein. By mapping the cross-linking residues, we determined the RNA–protein binding interface with single-residue resolution.

Results

To map the RNA–protein binding interface, we established a large-scale CR4/5-TRBD in vitro assembly system, consisting of purified TRBD protein and CR4/5 RNA fragments (Fig. 1 *A* and *B*). Recombinant medaka TRBD was overexpressed in *Escherichia coli* and purified as a fusion protein containing an N-terminal maltose-binding protein (MBP) tag for affinity purification (Fig. 1*C*). The RNA-binding affinity of the MBP–TRBD fusion protein was determined by a gel-mobility shift assay. The gel-mobility of the radiolabeled CR4/5 RNA fragment was retarded in the presence of MBP–TRBD (Fig. 1*D*). Using a filter-binding assay under a high-salt condition, we measured the K_d of recombinant MBP–TRBD to wild-type CR4/5 RNA as 0.55 ± 0.06 μM (Fig. 1*E*). Both the medaka CR4/5 RNA mutant lacking the conserved U bulge in the P6 stem and a human CR7 RNA fragment had no significant binding to MBP–TRBD (Fig. 1 *A* and *E*). We thus conclude the

This paper results from the Arthur M. Sackler Colloquium of the National Academy of Sciences, "Telomerase and Retrotransposons: Reverse Transcriptases That Shaped Genomes" held September 29–30, 2010, at the Arnold and Mabel Beckman Center of the National Academies of Sciences and Engineering in Irvine, CA. The complete program and audio files of most presentations are available on the NAS Web site at www.nasonline.org/telomerase_and_retrotransposons.

Author contributions: C.J.B. and J.J.-L.C. designed research; C.J.B., X.Q., and D.P.R. performed research; C.R.B. and R.W.N. contributed new reagents/analytic tools; C.J.B. and J.J.-L.C. analyzed data; and C.J.B. and J.J.-L.C. wrote the paper.

The authors declare no conflict of interest.

This article is a PNAS Direct Submission. N.F.L. is a guest editor invited by the Editorial Board.

[1]To whom correspondence should be addressed. E-mail: jlchen@asu.edu.

This article contains supporting information online at www.pnas.org/lookup/suppl/doi:10.1073/pnas.1100270108/-/DCSupplemental.

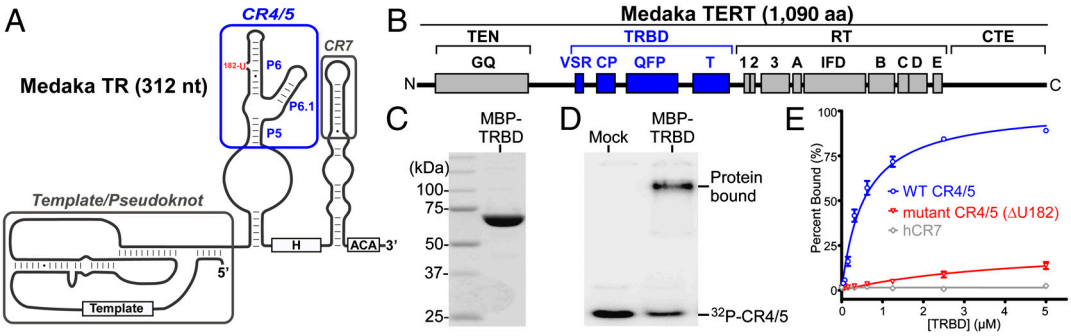

Fig. 1. Binding specificity between CR4/5 and TRBD. (*A*) Secondary structure of medaka TR. The CR4/5 domain is indicated by a blue box and the CR7 by a black box. The conserved U182 bulge in P6 helix is labeled in red. (*B*) Domain and motif organization of medaka TERT with TRBD motifs colored blue. (*C*) SDS-PAGE gel of purified MBP–TRBD fusion protein. (*D*) Gel-mobility shift assay of CR4/5-TRBD RNA–protein interaction. Protein-bound and free ^{32}P-CR4/5 RNA bands are indicated. (*E*) Binding curves of TRBD protein to wild-type (blue), mutant CR4/5 (ΔU182, red), and human TR CR7 (hCR7, gray) RNA fragments.

CR4/5-TRBD binding is specific and requires an intact CR4/5 structure.

We mapped the RNA–protein binding interface using a photoreagent-mediated cross-linking approach. The CR4/5 RNA containing photoaffinity cross-linker was prepared by in vitro T7 transcription in the presence of UTP and 5IU-5′-triphosphate at a ratio of 9:1 for partial and random labeling. Upon UV irradiation, the cross-linker 5IU becomes highly reactive and forms a covalent bond to an adjacent atom, typically from an aromatic amino acid (25). The 5IU-labeled CR4/5 RNA and TRBD protein fragments were assembled in vitro and irradiated with 302-nm UV light to generate RNA–protein cross-linked products (Fig. 2*A*, lanes 2–4). The cross-linked products were sensitive to trypsin protease treatment, indicating RNA–protein conjugates (Fig. 2*A*, lanes 4 and 5). The 5IU-mediated cross-linking generated a major product with an efficiency near 5% (Fig. 2*A*, lane 4 indicated by triangle). In contrast, a mock reaction using non-5IU RNA failed to generate this product (Fig. 2*A*, compare lanes 4 and 7). Incubation of TRBD protein with 4 μM tRNA, a nonspecific competitor, prior to CR4/5 binding did not reduce cross-linking efficiency (Fig. 2*B*, lane 3). Moreover, 5IU-labeled human CR7 RNA fragment also failed to cross-link to the medaka TRBD (Fig. 2*B*, lanes 4–6). Thus, the 5IU-mediated CR4/5-TRBD cross-linking was highly specific.

Alkaline partial hydrolysis was utilized to identify the cross-linking residues in the CR4/5 RNA. In this assay, the 5′-end ^{32}P-labeled RNA–protein conjugates were treated with a mild alkali, sodium carbonate, producing randomly cleaved RNA fragments. The largest radiolabeled non-peptide-linked RNA fragment in the ladder represented a product from the cleavage at the phosphodiester bond between the cross-linking and the 5′ neighboring nucleotides (Fig. 2*C*, denoted by −1). The partial hydrolysis analysis of the RNA–protein conjugates identified two cross-linking RNA residues, U182 and U205 (Fig. 2*D*). Reciprocal analysis using the 3′-end ^{32}P-labeled RNA–protein conjugates further confirmed both U182 and U205 as cross-linking residues (Fig. S1). In the secondary structure of the medaka CR4/5 domain, residues U182 and U205 are unpaired and would have the 5IU-labeled bases available for cross-linking to TRBD (Fig. 2*E*).

To determine the contribution of U182 and U205 for binding TRBD, the dissociation constant (K_d) of mutant CR4/5 RNAs, U182C and U205A/G207C, were each measured using filter-binding assay (Fig. S2). The U205A/G207C mutation was chosen for comparison to a similar double mutation in mouse TR that was previously found to have no effect on TERT binding (6). Similarly, the U205A/G207C mutation in medaka TR did not decrease binding affinity to the TRBD (Fig. S2). In contrast, mutation U182C slightly decreased binding affinity with an increased

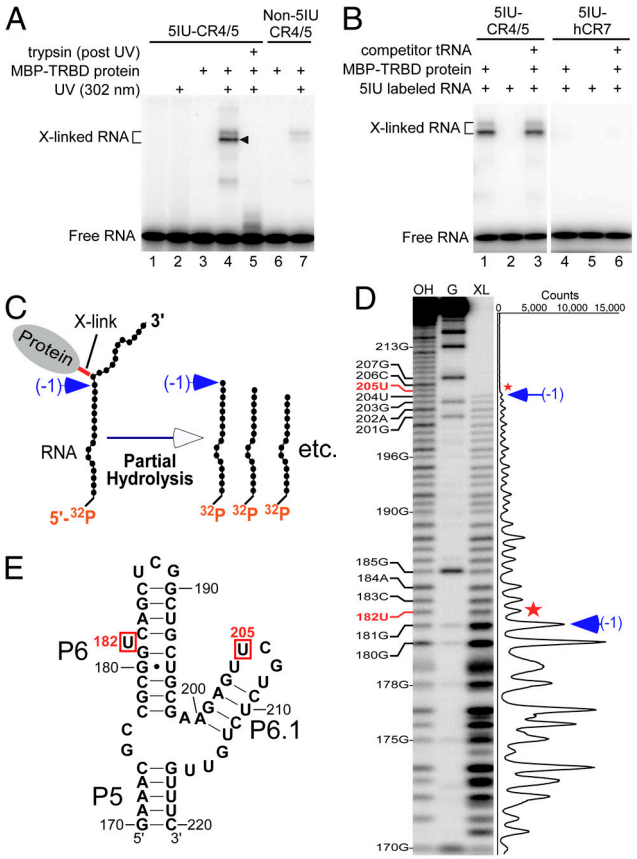

Fig. 2. Identification of cross-linking CR4/5 RNA residues. (*A*) The 5IU cross-linker mediates specific CR4/5-TRBD cross-linking. The CR4/5 RNA labeled with 5IU was incubated with MBP–TRBD protein and irradiated with 302-nm UV light (lane 4). Control reactions with no protein (lane 2), no UV treatment (lane 3), trypsin treatment (lane 5), or non-5IU-labeled RNA (lanes 6 and 7) are shown. (*B*) Competitor RNA failed to decrease CR4/5-TRBD cross-linking. Nonspecific competitor yeast tRNA was added to 4 μM (lanes 3 and 6). The 5IU-labeled human CR7 (hCR7) RNA failed to bind TRBD (lanes 4–6). (*C*) Schematic for identification of RNA cross-linking residues. Alkaline partial hydrolysis of 5′-end ^{32}P-labeled RNA-TRBD conjugate generates randomly cleaved RNA fragments. The longest labeled RNA fragment results from a cleavage between the cross-linked nucleotide and its 5′ adjacent nucleotide (−1, blue arrow). (*D*) PAGE analysis of partially hydrolyzed cross-linked CR4/5 RNA. An intensity trace of the TRBD cross-linked RNA (XL) lane is shown alongside the gel. The bands of the longest RNA fragments are indicated (−1, blue arrow). Red stars denote the cross-linking residues. Ladders: ^{32}P-labeled RNA hydrolyzed by alkaline (OH) or digested by RNase T1 (G). (*E*) Position of cross-linking uridines (red box) in the medaka CR4/5 secondary structure.

K_d of 1.4 μM from 0.55 μM (Fig. S2). Deletion of the U182 bulge drastically reduced binding affinity to near-background level. Thus, the U182 bulge is essential for TRBD binding.

To identify the amino acids cross-linked to U182 and U205, we employed MS to identify trypsinized TRBD peptides that were covalently linked to the RNA. RNA–protein conjugates were affinity-purified by the 6xHis tag at the C terminus of the recombinant MBP–TRBD using nickel-nitrilotriacetate agarose resin (Fig. S3*A*). Under denaturing conditions, this affinity purification step removed free un-cross-linked RNA. The MBP–TRBD protein was then digested with trypsin protease to generate small peptides. The RNA-peptide conjugates were gel-purified and digested with either RNase A or T1. The resulting oligonucleotide-peptide conjugates were then suitable for MALDI-TOF MS. A reference spectrum for MS analysis was generated from non-cross-linked (mock) RNA that was also RNase-treated and analyzed in parallel.

MALDI-TOF analysis of the RNase T1 digested RNA-peptide conjugate generated a single prominent peak at 2,380.1 Da (Fig. 3*A*). This peak was absent from the mock RNA reference spectrum, indicating a peptide-linked RNA fragment (Fig. 3*A*, compare upper and lower panels). Mass calculation of all possible combinations of trypsin-digested peptides and RNase T1-digested RNA fragments matched the 2,380.1-Da peak to peptide ^{496}FPPSELAYR^{504} and RNA fragment 5′-U^{182}CAG-3′ (Fig. 3*C*). Similar analysis of the RNaseA-treated sample identified two peaks at 2,091.1 and 2,395.9 Da, matching the same peptide ^{496}FPPSELAYR^{504} cross-linked to RNA fragments 5′-GGU^{182}-3′ and 5′-GGU^{182}C-3′, respectively (Fig. S3 *B* and *D*). The larger 5′-GGU182C-3′ fragment resulted from RNase A failing to cleave 3′ of U182, presumably due to the steric hindrance from the linked peptide. Mutation U182C eliminated the predominant ^{496}FPPSELAYR^{504} peptide peak, further confirming the cross-linking of U182 to this peptide. The U182C mutation increased the yield of the U205 cross-linked product. MALDI-TOF analysis of the U205 cross-linked peptide found the ^{470}ISVAELMWK^{478} peptide linked to an RNase T1-generated RNA fragment 5′-UU^{205}CG-3′ (Fig. 3 *B* and *C*). Analysis of the RNaseA-treated RNA sample confirmed the result from the RNase T1-treated sample (Fig. S3 *C* and *D*).

To identify the specific amino acids cross-linked to 5IU, we carried out MALDI-TOF/TOF tandem MS sequencing to detect collision-induced dissociation of amino acids and their derivatives from the parental peptide. Prior to MALDI-TOF/TOF analysis, the RNA-peptide sample was treated with alkali and phosphatase, generating peptides linked to a single uridine nucleoside.

The U182-linked peptide ^{496}FPPSELAYR^{504} has a mass of 1,321.61 Da (Fig. S4*A*). The MS/MS analysis of this nucleotide-peptide conjugate determined Tyr503 as the amino acid covalently bonded to U182 (Fig. 4*A*). The *b*-series ions from b_1 to b_7 had the expected peptide mass, whereas the b_8 ion had the increased mass of a uridine in addition to the tyrosine (Fig. 4*A*). In the *y* series, the y_2 ion had a similar increase in mass from uridine and tyrosine.

The U205-linked peptide ^{470}ISVAELMWK^{478} generated using the U182C mutant RNA had a mass of 1,318.63 Da (Fig. S4*B*). The MS/MS analysis of this nucleotide-peptide conjugate identified Trp477 covalently bonded to U205 (Fig. 4*B*). An additional peak was observed at 1,334.62 Da, which is 16 Da larger than the expected mass (Fig. S4*B*, *Inset*). MS/MS analysis confirmed this was the same ^{470}ISVAELMWK^{478} peptide but with an oxidized methionine accounting for the mass increase.

A third nucleotide-peptide conjugate peak was observed at 2,024.9 Da, which matched to the mass of the peptide ^{352}LVFFEGLPYLNGQER^{366} and a uridine (Fig. S4*A*). The MS/MS analysis of this peptide identified Phe355 as the cross-linked amino acid to an unidentified uridine from the CR4/5 RNA (Fig. 4*C*). Alkaline partial hydrolysis and MALDI-TOF analysis of the trypsin/RNase-treated conjugate failed to identify the third cross-linking nucleotide, presumably due to the large size of the peptide (Fig. 3 and Fig. S3). Double-protease digestion using trypsin and chymotrypsin further cleaved the RNase T1-treated RNA-peptide conjugate to a single phenylalanine-RNA conjugate. MALDI-TOF analysis of this sample identified a 1,442.0-Da peak that matched to the mass of a single phenylalanine and an RNA fragment 5′-CUCG-3′ from loop L6 (Fig. S5 *A*–*C*). This result suggests the U187 residue in loop L6 is the third cross-linking nucleotide. Moreover, CR4/5 RNA mutations that removed P5 or mutated the unpaired U residues in the three-way-junction did not eliminate the 2,025-Da peak of the U-linked peptide ^{352}LVFFEGLPYLNGQER^{366} conjugate, further supporting U187 as the nucleotide cross-linking to Phe355 (Fig. S5 *D*–*F*).

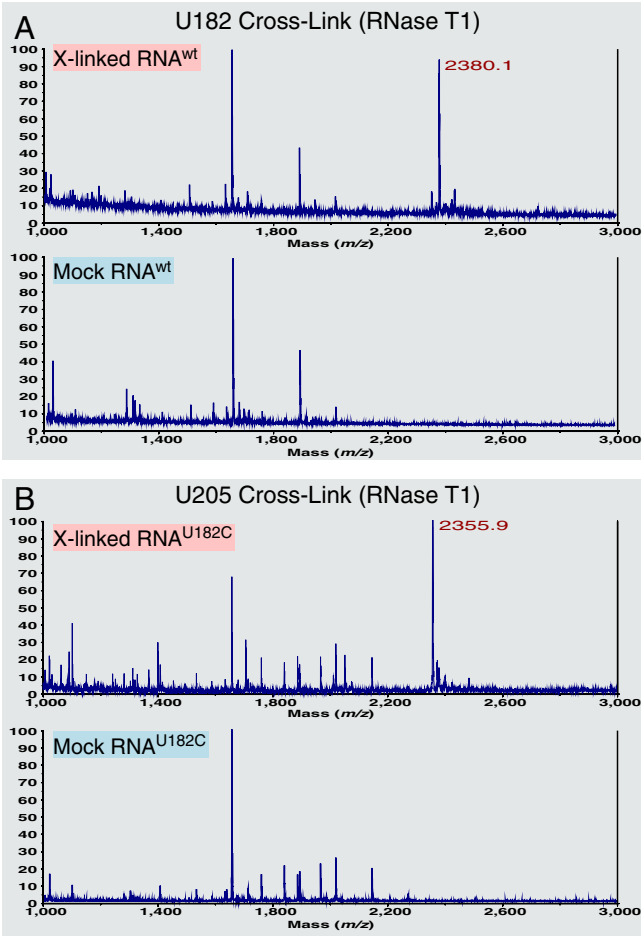

C

Cross-link Site	Peptide [M]	RNA [M]	[M+H] calc.	[M+H] exp.
U182	FPPSELAYR 1078.6	UCAG 1303.2	2380.8	2380.1
U205	ISVAELMWK 1075.6	UUCG 1280.1	2354.7	2355.9
	a	b	=a+b-1	

Fig. 3. Identification of cross-linked RNA-peptide conjugates. (*A*) MALDI-TOF MS spectrum of trypsin/RNase T1 digested RNA-peptide conjugate (X-linked) or un-cross-linked RNA (mock). Peak of cross-linked products is indicated in red. (*B*) MALDI-TOF MS of U205-cross-linked RNA-peptide conjugate. The U205 cross-linked RNA-peptide conjugate was generated using the U182C mutant RNA. (*C*) Sequence and mass of the RNA-peptide conjugates. Calculated (calc.) and experimental (exp.) masses of the RNA-peptide conjugates are shown. Calculated mass is adjusted for the loss of a hydrogen during both 5IU labeling and cross-linking as well as the gain of a hydrogen from the positive-ion MS analysis.

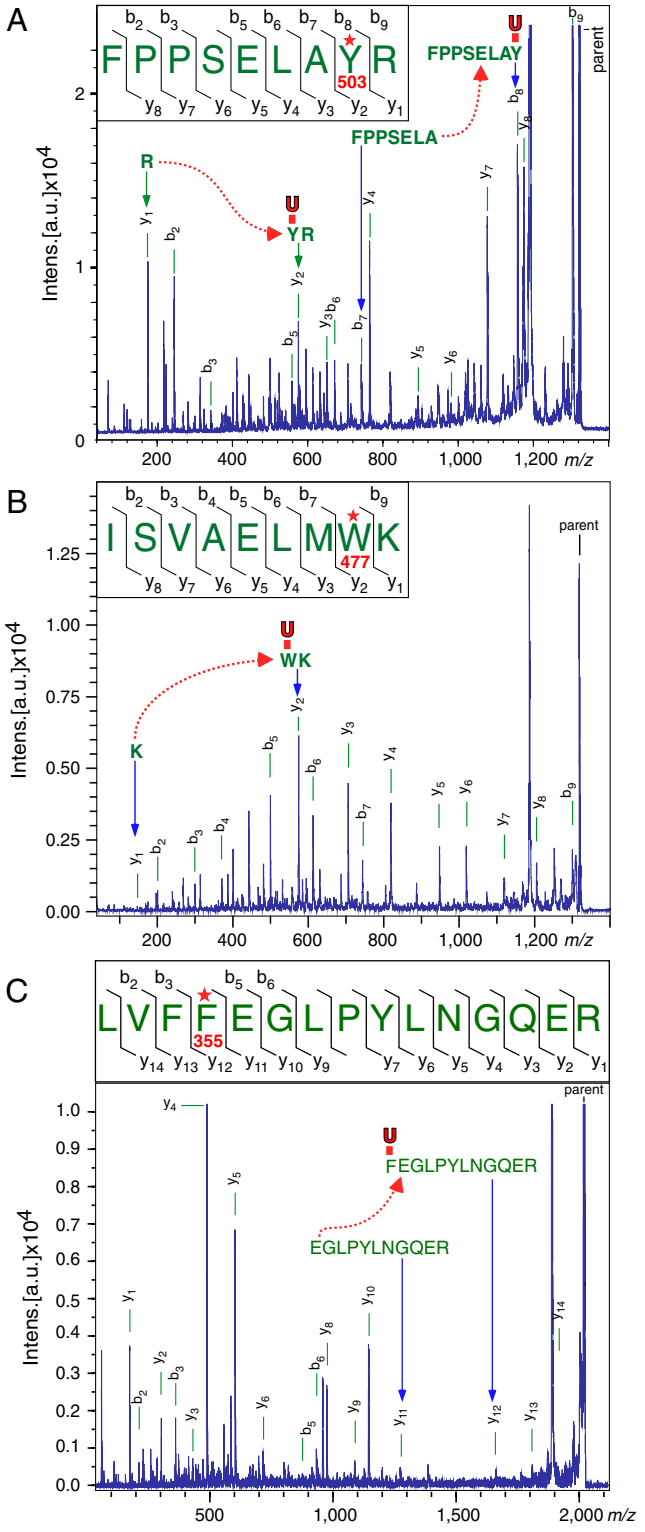

Fig. 4. Identification of the cross-linked amino acids in RNA-peptide conjugates. (*A*) MALDI-TOF/TOF tandem MS sequencing of U182-linked peptide. The peaks of *b*- and *y*-series ions are labeled. Inset details the *b* and *y* ion fragments observed in the peptide-sequencing spectrum with the uridine-linked residue indicated by a red star. The large mass shifts from y_1 to y_2, and from b_7 to b_8, resulting from cross-linking to a uridine are indicated. (*B*) Sequencing of U205-linked peptide. The fragmentation pattern observed is indicated in the sequence shown in inset. (*C*) Sequencing of the third uridine-linked peptide. MALDI-TOF/TOF analysis confirmed deamination of Asn362 with a 1-Da mass shift of in the *y* ion series between y_4 and y_5 when compared to expected masses of unmodified peptide.

The contribution of the cross-linking residues, Phe355, Trp477, and Tyr503, in binding the CR4/5 RNA was examined by mutagenesis. These aromatic residues were each substituted with an aromatic or nonaromatic amino acid, and analyzed for RNA-binding affinity. Mutants with aromatic substitutions, Trp477Phe and Tyr503Phe, retained wild-type RNA-binding affinity, whereas mutants with nonaromatic substitutions, Trp477Leu and Tyr503-Ser, showed reduced binding affinity (Fig. S6*A*). For Phe355, substitutions Phe355Tyr and Phe355Leu both reduced RNA-binding affinity (Fig. S6*A*). In the context of the full-length TERT protein, these mutations exhibited similar effects for CR4/5 RNA-binding affinity (Fig. S6*B*). As expected, these TERT mutations did not affect pseudoknot RNA binding. Activity assay of these mutants showed reduced telomerase activity for the Phe355 and Tyr503 mutants, and reduced repeat addition processivity for the Trp477 mutant (Fig. S6*C*). Because Trp477 is in close proximity to the L6.1 loop of CR4/5 RNA, we assayed the L6.1 mutant U205A/G207C for telomerase activity and processivity. The L6.1 mutation decreased telomerase activity but surprisingly increased repeat addition processivity (Fig. S6*D*). These results indicate that these three amino acids are important for both CR4/5 RNA binding and telomerase activity.

Reciprocally, we determined the CR4/5 structural elements essential for binding TRBD. An array of CR4/5 RNA substitutions and truncations were examined by filter-binding assay (Fig. S7*A*). The results suggest stems P6, P6.1, and loop L6 are important for binding TRBD (Fig. 5*A* and Fig. S7*B*). In contrast, substitution of conserved nucleotides in L6.1 had no effect on binding TRBD (Fig. S7*B*, mutant M6), which is consistent with a previous study on mouse TR (6). Truncations of CR4/5 RNA showed stem P5 is not necessary for TRBD binding (Fig. S7*B*, mutants M10–11), in accordance with a previous study that also showed P5 is dispensable for reconstituting telomerase activity in vitro (26). The minimal RNA fragment that retained wild-type binding affinity is only 39 nt, spanning residue 176 to residue 214. Although the P5 stem is not essential, specific residues in the internal loop of the three-way helical junction are required for effective TRBD binding (Fig. S7*B*, mutants M11–15). This functional survey of RNA mutations and truncations determined the essential TRBD-binding region within the CR4/5 domain (Fig. 5*A*).

To predict positions on the TERT structure, residues Trp477, Tyr503, and Phe355 were mapped onto a medaka TRBD struc-

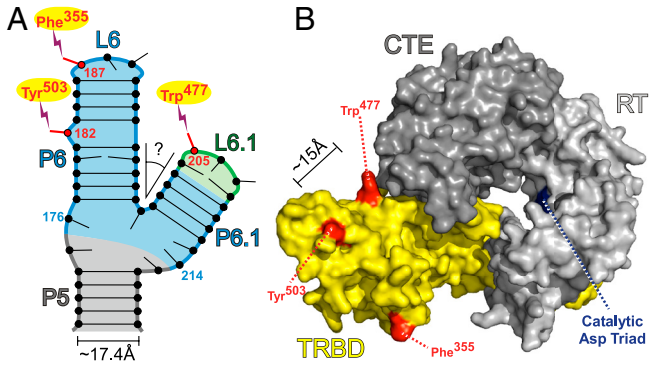

Fig. 5. Positions of cross-linking residues on the CR4/5 and TRBD structures. (*A*) The cross-linking nucleotides (U182, U187, and U205) are labeled on the CR4/5 secondary structure with the corresponding amino acids, Tyr503, Phe355, and Trp477, as indicated. The structure of CR4/5 is divided into regions necessary for TRBD binding (shaded blue), necessary for enzymatic activity (shaded green), and dispensable for either (shaded gray). The diameter of the A-form RNA helix is about 17.4 Å measured from phosphate to phosphate. (*B*) Superimposition of the Medaka TRBD threading-based model (yellow) on the *Tribolium* TERT structure (RT domain, light gray; CTE domain, dark gray). Cross-linked residues Phe355, Trp477, and Tyr503 are colored red. The catalytic aspartate triad in the RT domain is labeled (blue). On the structural model, Trp477 and Tyr503 are separated by about 15 Å.

tural model (Fig. 5*B*). This homology model was generated by threading the medaka sequence through the *Tetrahymena* TRBD crystal structure (Fig. S8 *A–D*). It is noted that the actual medaka structure may differ from either the *Tetrahymena* structure or medaka threading-based TRBD model. Nonetheless, superimposition of the *Tetrahymena* structure and the medaka model with the *Tribolium* TERT structure suggested similar protein folds for all three structures (Fig. S8 *E* and *F*). Moreover, based on sequence alignment and secondary structure prediction, Trp477 and Tyr503 were mapped to similar positions on both *Tetrahymena* and *Tribolium* TRBD structures. In comparison, the third residue Phe355 is located in the vertebrate-specific VSR motif, making the prediction of its position in the structure more difficult (Fig. S8 *C–E*). Both the *Tetrahymena* and *Tribolium* structures, as well as the medaka model, have a positively charged surface patch where the CR4/5 cross-linking amino acids are located (Fig. S8*D*). The positions of these cross-linked residues in relation to the RT and CTE domains are shown on a combined model that superimposed the medaka TRBD model and *Tribolium* TERT structures (Fig. S8*E*). The TRBD structural models together with the mapped CR4/5 binding surface provide useful insights into the role of CR4/5-TRBD interaction in telomerase function.

Discussion

Functional assembly of the vertebrate telomerase RNP relies on specific RNA–protein interactions between TR and TERT (6, 24, 27). The template-pseudoknot domain binds to the TEN domain, positioning the template within the TERT active site, and defines the template boundary (10, 28, 29). The CR4/5 domain binds to the TRBD with a critical yet enigmatic function for enzymatic activity. Mutagenesis and functional analyses have suggested several possible functions for CR4/5-TRBD binding: facilitating a conformational activation of TRBD (18), interacting with RNA template (30), or enhancing enzymatic catalysis (6, 27, 31). Our photoaffinity cross-linking analysis has defined the CR4/5-TRBD binding interface, providing insight into the assembly of the telomerase RNP and the function of the critical CR4/5 domain.

The CR4/5 elements required for TRBD binding include: stems P6 and P6, loop L6, and the three-way-junction internal loop (Fig. S7). The single-nucleotide U182 bulge in P6.1 and the 5-nucleotide loop L6.1 are structural features universally conserved in all known vertebrate TRs, suggesting crucial roles in telomerase function (7, 24). The U182 bulge within stem P6 is essential for TRBD binding because deletion of this residue nearly abolishes binding affinity (Figs. S2 and S7*B*). However, deletion of this bulge may also affect the tertiary structure of the entire stem loop and thus reduce TRBD binding. Although our cross-linking data do not provide direct evidence for physical interactions, they outline the RNA–protein binding interface between CR4/5 and TRBD.

Stem-loop 6.1 is the most highly conserved element in the CR4/5 domain (7, 24). Stem P6.1 is essential for TRBD binding, whereas loop L6.1 is not (Fig. S7*B*). Although the cross-linking data indicate U205 and Trp477 are in immediate proximity, these two residues may not form critical contacts. Loop L6.1 is highly conserved in all vertebrates and crucial for telomerase activity and repeat addition processivity (Fig. S6*D*). Mapping the U205 cross-linked amino acid Trp477 onto the medaka TRBD model places L6.1 in close proximity to the adjoining CTE domain and distant from the catalytic RT domain (Fig. 5*B*). We therefore conclude that L6.1 does not directly participate in catalysis. Instead, the position of this loop suggests that this structure may facilitate functional folding of TERT through a putative interaction with CTE. This putative L6.1–CTE interaction may be required for functional folding or assembly of active telomerase RNP, which would explain the requirement of CR4/5 for reconstituting telomerase activity (Fig. S6*D*, lane 2). Because mutations in the CTE domain affect repeat addition processivity (32, 33), the altered processivity of the Trp477Leu and L6.1 (U205A/G207C) mutants are potentially mediated by this putative L6.1-CTE interaction. A recent study suggested that, in human telomerase, the TRBD and CTE domains interact in the absence of TR (28). However, CR4/5 might provide additional and crucial interactions to CTE for proper positioning of the CTE domain and optimal assembly of the telomerase RNP.

The spacing of the three cross-linked residues in TRBD together with the secondary structure of CR4/5 provides a glimpse to the tertiary orientation of stems P6 and P6.1. Measuring within the two known structures and a medaka threading-based model of TRBD, the two cross-linking sites of U182 and U205 are separated by only 15–20 Å (Fig. 5*B*), suggesting that the U bulge of P6 and L6.1 are close to each other, requiring a sharp turn at the junction (Fig. 5*A*). This evidence argues against a coaxial stacking of these two helices as suggested in previous reports (34, 35).

The highly conserved TRBD motifs, QFP, CP, and T, have little overlap with the CR4/5 binding surface (Fig. S8*C*), suggesting that these motifs have other functions than binding the CR4/5 RNA. Motif T is part of the T pocket, a previously proposed RNA-binding site that has a positively charged surface (22). The T pocket is located near the active site and potentially interacts with the RNA template and/or template boundary elements. In support of this interaction, mutations in motif T affect the repeat addition rate (36). The U182 cross-linked residue Trp477 participates in RNA binding and is located at the C terminus of motif QFP (Fig. S8 *A* and *C*). The remaining QFP may stabilize protein folding, as suggested by the *Tribolium* TERT structure (23). Motif CP is located opposite the CR4/5 binding pocket (Fig. S8*C*). Deletion of this motif completely abolishes telomerase activity, whereas RNA binding is only slightly reduced (9). The vertebrate-specific motif VSR contains the third cross-linked residue Phe355 and is part of the CR4/5 binding pocket. However, VSR may interact with a vertebrate-specific TR element and may not be conserved in other species. In general, there is less sequence conservation in the CR4/5 binding interface than in the three motifs, CP, QFP, and T, presumably because of a rapid coevolution of the TERT with the divergent TR.

The integral RNA component and its interacting protein domains are unique features that distinguish the telomerase RNP from retrotransposons. Mapping the RNA–protein binding interface between the CR4/5 and TRBD provides important clues for the assembly of TR and TERT into a functional RNP, and a potential function for the essential CR4/5 domain. Moreover, the methodology developed in this study for mapping a telomerase RNA–protein binding interface can be adapted and applied to other species, as well as other RNP complexes.

Materials and Methods

Protein Expression and Purification. A synthetic medaka RNA-binding domain (TRBD) gene (encoding for amino acids 318–579) was cloned into pMAL-2CX (New England Biolabs) generating plasmid pMBP-TRBD-6xHis. The recombinant protein gene was expressed in ScarabXpress T7lac cells (Scarab Genomics). Cells were lysed by sonication in 1× column buffer [50 mM Tris·HCl (pH 7.5), 500 mM NaCl, 1 mM $MgCl_2$ 10% glycerol, and 1 mM tris(2-carboxyethyl)phosphine (TCEP)] supplemented with 1 mM PMSF and 1× complete protease inhibitor cocktail (Roche). Lysate was centrifuged at 18,000 × *g* for 15 min followed by 55% ammonium sulfate precipitation. The pellet was resuspended in 1× column buffer, applied to amylose resin (New England Biolabs) and eluted with 10 mM maltose. Peak fractions were pooled and applied to a gel filtration column (Sephadex 200; GE). Eluted MBP–TRBD monomer was used for further studies.

Gel-Mobility Shift Assay. Equal molar ^{32}P 5′-labeled CR4/5 RNA and purified MBP–TRBD fusion protein were mixed at 0.8 μM and incubated in 20 μL column buffer at room temperature for 30 min. Ten microliters of the binding reaction was loaded onto a native polyacrylamide gel [5% acrylamide:bisacrylamide (29:1), 0.5× TBE (45 mM Tris·HCl, 45 mM boric acids, and 1 mM EDTA, pH 8.0), 5% glycerol, and 1 mM $MgCl_2$] for electrophoresis, and the

dried gel was exposed to a storage phosphor screen for image analysis with PhosphorImager FX-Pro (BioRad).

Filter-Binding Assay. Radiolabeled RNA (*ca.* 0.5 nM) was incubated with purified MBP–TRBD protein from 50 nM to 5 μM in 1× binding buffer [50 mM Tris·HCl (pH 7.5), 500 mM NaCl, 1 mM $MgCl_2$ 10% glycerol, and 1 mM TCEP) at room temperature for 30 min. Aliquots of the RNA–protein mixtures were applied onto prewashed 0.2 μM Protran (BA83) nitrocellulose membranes (Whatman) on a 1225 Sampling Manifold (Millipore) under vacuum. The membranes were washed once with 1 mL 1× binding buffer. The dried membranes were exposed to a storage phosphor screen and analyzed using the Molecular Imager FX-Pro (BioRad). Intensity of RNA bound on each membrane was quantitated by Quantity One software (BioRad) and normalized to the input RNA. Binding titrations were performed in triplicate. K_d and SEM were determined using the one-site-specific binding function in Prism 5 (GraphPad Software).

Photoaffinity Cross-linking Analysis and RNA Cross-linking Residue Identification. RNA was in vitro transcribed in the presence of UTP and 5-iodouridine 5′-triphosphate (Trilink) at a ratio of 9:1, gel extracted, and 5′ radiolabeled by ^{32}P-γ-ATP and T4 polynucleotide kinase (New England Biolabs). Two nanograms of RNA and approximately 23 μg of MBP–TRBD protein were incubated on ice for 30 min in 50 μL of 1× binding buffer [50 mM Tris·HCl (pH 7.5), 500 mM NaCl, 1 mM $MgCl_2$ 10% glycerol, and 1 mM tris(2-carboxyethyl)phosphine], and then irradiated with 302-nm UV light for 2 h. The sample was then electrophoresed on an 8% SDS gel followed by autoradiography. The cross-linking residues in the RNA were identified using alkaline partial hydrolysis as previously described with minor modifications (37). In brief, gel slices containing the cross-linked RNA were excised, washed three times with 1 mL water, and incubated in 100 μL hydrolysis buffer [100 mM sodium carbonate (pH 9.5) and 1 mM EDTA] for 5 min at room temperature and 10 min at 90 °C. Reaction was neutralized by 200 μL of 100 mM Tris·HCl (pH 7.5), and RNA was eluted overnight and ethanol precipitated. Partially hydrolyzed RNA fragments were resolved on a denaturing 10% polyacrylamide sequencing gel along with both RNase T1-digested and alkaline-hydrolyzed RNA ladders.

Additional materials and methods for TRBD protein purification, filter-binding assay, telomerase activity assay, and cross-linking residue identification using mass spectrophotometry are described in *SI Materials and Methods*.

ACKNOWLEDGMENTS. We thank Joshua Podlevsky and René Davis for critical reading of the manuscript. This work was supported by National Sciences Foundation Career Award MCB0642857 (to J.J.-L.C.).

1. Greider CW, Blackburn EH (1985) Identification of a specific telomere terminal transferase activity in Tetrahymena extracts. *Cell* 43:405–413.
2. Armanios M (2009) Syndromes of telomere shortening. *Annu Rev Genomics Hum Genet* 10:45–61.
3. Kim NW, et al. (1994) Specific association of human telomerase activity with immortal cells and cancer. *Science* 266:2011–2015.
4. Greider CW, Blackburn EH (1989) A telomeric sequence in the RNA of Tetrahymena telomerase required for telomere repeat synthesis. *Nature* 337:331–337.
5. Theimer CA, Blois CA, Feigon J (2005) Structure of the human telomerase RNA pseudoknot reveals conserved tertiary interactions essential for function. *Mol Cell* 17:671–682.
6. Chen J-L, Opperman KK, Greider CW (2002) A critical stem-loop structure in the CR4-CR5 domain of mammalian telomerase RNA. *Nucleic Acids Res* 30:592–597.
7. Chen J-L, Blasco MA, Greider CW (2000) Secondary structure of vertebrate telomerase RNA. *Cell* 100:503–514.
8. Mitchell JR, Collins K (2000) Human telomerase activation requires two independent interactions between telomerase RNA and telomerase reverse transcriptase. *Mol Cell* 6:361–371.
9. Moriarty TJ, Huard S, Dupuis S, Autexier C (2002) Functional multimerization of human telomerase requires an RNA interaction domain in the N terminus of the catalytic subunit. *Mol Cell Biol* 22:1253–1265.
10. Moriarty TJ, Marie-Egyptienne DT, Autexier C (2004) Functional organization of repeat addition processivity and DNA synthesis determinants in the human telomerase multimer. *Mol Cell Biol* 24:3720–3733.
11. Friedman KL, Cech TR (1999) Essential functions of amino-terminal domains in the yeast telomerase catalytic subunit revealed by selection for viable mutants. *Genes Dev* 13:2863–2874.
12. Xia J, Peng Y, Mian IS, Lue NF (2000) Identification of functionally important domains in the N-terminal region of telomerase reverse transcriptase. *Mol Cell Biol* 20:5196–5207.
13. Bosoy D, Peng Y, Mian IS, Lue NF (2003) Conserved N-terminal motifs of telomerase reverse transcriptase required for ribonucleoprotein assembly in vivo. *J Biol Chem* 278:3882–3890.
14. Bryan TM, Goodrich KJ, Cech TR (2000) Telomerase RNA bound by protein motifs specific to telomerase reverse transcriptase. *Mol Cell* 6:493–499.
15. Brown Y, et al. (2007) A critical three-way junction is conserved in budding yeast and vertebrate telomerase RNAs. *Nucleic Acids Res* 35:6280–6289.
16. Mason DX, Goneska E, Greider CW (2003) Stem-loop IV of tetrahymena telomerase RNA stimulates processivity in trans. *Mol Cell Biol* 23:5606–5613.
17. Lai CK, Miller MC, Collins K (2002) Template boundary definition in Tetrahymena telomerase. *Genes Dev* 16:415–420.
18. Robart AR, O'Connor CM, Collins K (2010) Ciliate telomerase RNA loop IV nucleotides promote hierarchical RNP assembly and holoenzyme stability. *RNA* 16:563–571.
19. Lai CK, Miller MC, Collins K (2003) Roles for RNA in telomerase nucleotide and repeat addition processivity. *Mol Cell* 11:1673–1683.
20. Stone MD, et al. (2007) Stepwise protein-mediated RNA folding directs assembly of telomerase ribonucleoprotein. *Nature* 446:458–461.
21. O'Connor CM, Lai CK, Collins K (2005) Two purified domains of telomerase reverse transcriptase reconstitute sequence-specific interactions with RNA. *J Biol Chem* 280:17533–17539.
22. Rouda S, Skordalakes E (2007) Structure of the RNA-binding domain of telomerase: Implications for RNA recognition and binding. *Structure* 15:1403–1412.
23. Gillis AJ, Schuller AP, Skordalakes E (2008) Structure of the Tribolium castaneum telomerase catalytic subunit TERT. *Nature* 455:633–637.
24. Xie M, et al. (2008) Structure and function of the smallest vertebrate telomerase RNA from teleost fish. *J Biol Chem* 283:2049–2059.
25. Meisenheimer KM, Koch TH (1997) Photocross-linking of nucleic acids to associated proteins. *Crit Rev Biochem Mol Biol* 32:101–140.
26. Kim NK, et al. (2010) Effect of pseudouridylation on the structure and activity of the catalytically essential P6.1 hairpin in human telomerase RNA. *Nucleic Acids Res* 38:6746–6756.
27. Robart AR, Collins K (2010) Investigation of human telomerase holoenzyme assembly, activity, and processivity using disease-linked subunit variants. *J Biol Chem* 285:4375–4386.
28. Robart AR, Collins K (2011) Human telomerase domain interactions capture DNA for TEN domain-dependent processive elongation. *Mol Cell* 42:308–318.
29. Moriarty TJ, Marie-Egyptienne DT, Autexier C (2005) Regulation of 5′ template usage and incorporation of noncognate nucleotides by human telomerase. *RNA* 11:1448–1460.
30. Ueda CT, Roberts RW (2004) Analysis of a long-range interaction between conserved domains of human telomerase RNA. *RNA* 10:139–147.
31. Blackburn EH, Collins K (2011) Telomerase: An RNP enzyme synthesizes DNA. *Cold Spring Harb Perspect Biol* 3:a003558.
32. Qi X, et al. (2011) RNA/DNA hybrid binding affinity determines telomerase template-translocation efficiency. *EMBO J*, 10.1038/emboj.2011.363.
33. Xie M, et al. (2010) A novel motif in telomerase reverse transcriptase regulates telomere repeat addition rate and processivity. *Nucleic Acids Res* 38:1982–1996.
34. Leeper TC, Varani G (2005) The structure of an enzyme-activating fragment of human telomerase RNA. *RNA* 11:394–403.
35. Leeper T, Leulliot N, Varani G (2003) The solution structure of an essential stem-loop of human telomerase RNA. *Nucleic Acids Res* 31:2614–2621.
36. Drosopoulos WC, Prasad VR (2009) Telomerase-specific T motif is a restrictive determinant of repetitive reverse transcription by human telomerase. *Mol Cell Biol* 30:447–459.
37. Hiley SL, Sood VD, Fan J, Collins RA (2002) 4-thio-U cross-linking identifies the active site of the VS ribozyme. *EMBO J* 21:4691–4698.

Supporting Information

Bley et al. 10.1073/pnas.1100270108

SI Materials and Methods

MALDI-TOF Mass Spectrometry. Prior to cross-linking, 3 μM of purified maltose-binding protein (MBP)–telomerase RNA-binding domain (TRBD)-6xHis fusion protein and 3 μM of in vitro transcribed CR4/5 RNA were incubated in 1 mL of 1× binding buffer [50 mM Tris·HCl (pH 7.5), 500 mM NaCl, 1 mM $MgCl_2$ 10% glycerol, and 1 mM tris(2-carboxyethyl)phosphine] at room temperature for 30 min. Cross-linking was performed using a handheld 302-nm UV lamp (Ultraviolet Products, Ltd.) on ice for 2 h. Undesirable sub-300-nm UV light was blocked by a polystyrene filter. Following cross-linking, sample was denatured with 3 vol of denaturing buffer [8 M urea, 250 mM NaCl, 100 mM sodium phosphate (pH 8.0), 10 mM Tris·HCl (pH 8.0), and 0.1% Triton X-100], and the RNA–protein conjugates were affinity-purified with 0.4 mL Ni-nitrilotriacetate resin (Qiagen). Following overnight incubation at room temperature, the resin was washed three times with 2 mL denaturing buffer and twice with water. Sample was digested with 20 μg sequencing-grade trypsin (Promega) in 400 μL trypsin digestion buffer (25 mM ammonium bicarbonate and 1 M urea) at 37 °C overnight. The trypsin-digested sample was mixed with 2× formamide loading buffer [10 mM Tris·HCl (pH 8.0), 20 mM EDTA, 0.01% bromophenol blue, 0.01% xylene cyanol, and 80% formamide], and electrophoresed on a denaturing 4% polyacrylamide/8 M urea gel to purify the peptide-RNA conjugate. Non-cross-linked (mock) RNA was also loaded separately as negative control. The RNA-containing bands were visualized by UV shadowing, excised, and eluted overnight in 2.5 M ammonium acetate at pH 5.2. Samples were ethanol precipitated, resuspended in water, and treated with 0.2 μg RNase A (GenScript) or 40 units RNase T1 (Ambion) in 10 mM TEAA (triethylammonium acetate, pH 7.0) buffer at 50 °C for 1 h. Prior to mass spectrometry, the digested RNA-peptide conjugates were purified with a μC18 ZipTip (Millipore) following the manufacture's instructions for oligonucleotides. One microliter of purified sample in 50% acetonitrile/0.1% TFA was mixed with 2 μL saturated 3-hydroxy picolinic acid matrix, and analyzed using a Voyager-DE STR MALDI-TOF Workstation (Applied Biosystems) in positive-ion-reflectron mode.

MALDI-TOF/TOF Tandem Mass Spectrometry. The cross-linked peptide sample was prepared as described above for MALDI-TOF analysis, amended with alkaline hydrolysis in place of RNase digestion. Alkaline hydrolysis was performed in 5% vol/vol ammonia solution at 90 °C overnight. Ammonia was removed by evaporation in a Speedvac (Thermo Scientific). The dehydrated sample was resuspended in 30 μL water, dehydrated again, and resuspended in 30 μL 0.1 M TEAA. The sample was incubated with 1 unit of alkaline phophatase (New England Biolabs) at 50 °C for 30 min and purified using a μC18 ZipTip. One microliter of purified sample in 50% acetonitrile/0.1% TFA was mixed with 2 μL saturated α-cyano-4-hydroxycinnamic acid and analyzed on an Ultraflex III MALDI-TOF/TOF Mass Spectrometer (Bruker Daltonics).

Telomerase in Vitro Reconstitution and Telomerase Activity Assay. Full-length medaka telomerase reverse transcriptase (TERT) (FLAG-mdTERT) was expressed in rabbit reticulocyte lysate (RRL) using TNT T7 Quick Coupled Transcription/Translation System (Promega) following the manufacturer's instruction. Medaka telomerase was reconstituted by adding 1 μM medaka telomerase RNA (TR) pseudoknot fragment (residues 1–150) and 50 nM of CR4/5 fragment (residues 170–220) in 10 μL RRL reaction of TERT synthesis, and incubated at 30 °C for 30 min. The conventional telomerase direct activity assay was carried out in 10 μL reactions with 2 μL in vitro reconstituted telomerase in the presence of 1× PE buffer [50 mM Tris·HCl (pH 8.3), 2 mM DTT, 0.5 mM $MgCl_2$, and 1 mM spermidine], 1 mM dATP, 1 mM dTTP, 50 μM dGTP, 0.167 μM of α-^{32}P-dGTP, and 1 μM $(TTAGGG)_3$ at 30 °C for 1 h. Telomerase activity assay products were phenol/chloroform extracted, ethanol precipitated, and resolved in a 10% denaturing PAGE gel. The gel was dried and exposed to a storage phosphor screen for image analysis with phosphorimager FX-Pro (BioRad). Telomerase activity and processivity were quantitated as previously described (1).

TERT and TR Binding Assay. Radioactive ^{35}S-labeled FLAG-mdTERT and 10 nM ^{32}P-end-labeled pseudoknot and CR4/5 RNA fragments were incubated in 25 μL RRL reaction at 30 °C for 10 min. Immunoprecipitation of FLAG-mdTERT was carried out by mixing RRL reactions with 10 μL anti-FLAG M2 affinity agarose beads (Sigma) and incubating at 4 °C for 2 h. After centrifugation at 1,000 × *g* for 30 s, 1 μL of supernatant was taken as the unbound fraction. After washing three times with 1× Tris buffered saline (50 mM Tris·HCl at pH 7.4 and 150 mM NaCl), the beads were aliquoted equally into two tubes for RNA and protein analyses. RNA samples bound to the beads were extracted with 2× formamide loading buffer and resolved in a 4% polyacrylamide/8 M urea denaturing gel. Proteins bound to the beads were dissolved in 2× Laemmli buffer [0.25 M Tris·HCl (pH 6.8), 4% SDS, 20% glycerol, 10% BME, and 0.005% bromophenol blue] and resolved in a 6% SDS-PAGE gel. The gels were dried and exposed to storage phosphor screen for image analysis with PhosphorImager FX-Pro (BioRad).

1. Xie M, et al. (2008) Structure and function of the smallest vertebrate telomerase RNA from teleost fish. *J Biol Chem* 283:2049–2059.

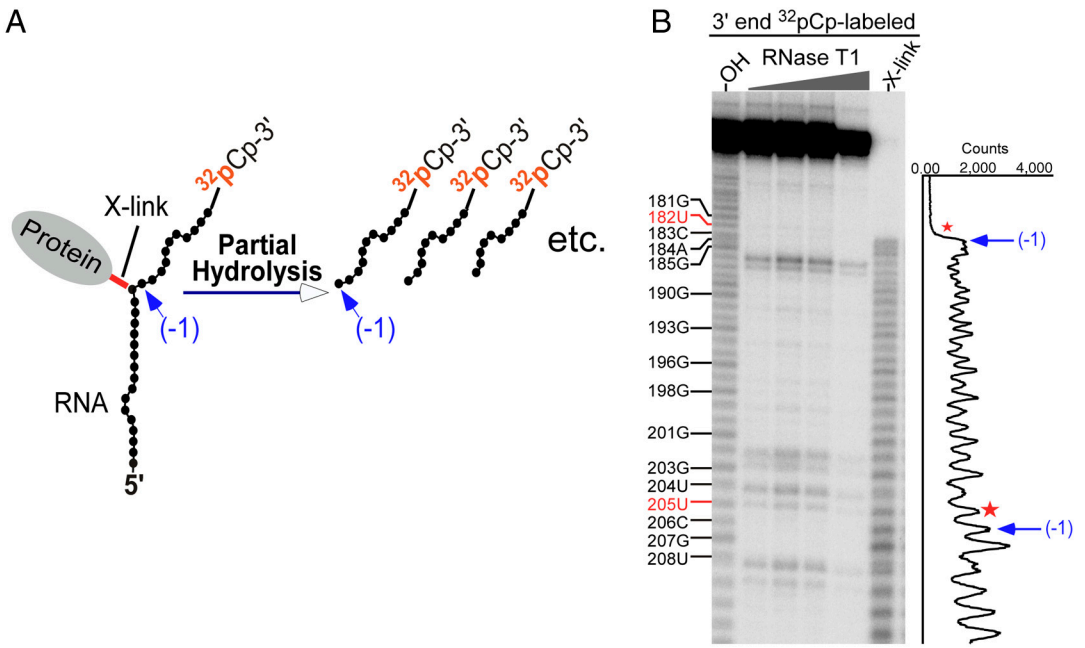

Fig. S1. Alkaline partial hydrolysis for mapping cross-linking RNA residues using 3′-end ^{32}P-labeled CR4/5 RNA. (*A*) Schematic of alkaline partial hydrolysis of the protein cross-linked RNA 3′-end labeled with ^{32}pCp. The longest RNA fragment generated from alkaline partial hydrolysis represents cleavage of the phosphodiester bond between the cross-linked nucleotide and the 3′ adjacent nucleotide (−1, blue arrow). (*B*) PAGE analysis of partially hydrolyzed cross-linked 3′-end ^{32}pCp labeled CR4/5 RNA. An intensity trace of bands in the TRBD cross-linked RNA (X-link) lane is shown alongside the gel with the longest RNA fragment indicated (−1, blue arrow) and the cross-linking fragment (red star). Ladders: alkaline-hydrolyzed (OH) and RNase T1-digested (RNase T1) 3′-end-labeled RNA. The sequence of the RNA fragment is shown alongside the gel.

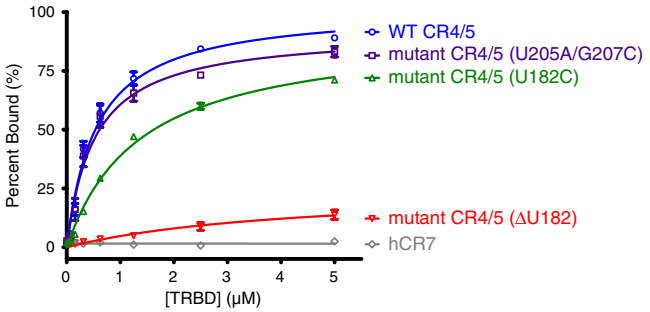

Fig. S2. TRBD-binding assay of CR4/5 RNA mutants. TRBD-binding affinity of CR4/5 RNA mutants (ΔU182, U182C, and U205A/G207C) was measured by filter-binding assay. Human CR7 (hCR7) RNA was included as a negative control. RNA labeled with ^{32}P at 5′ end was incubated with increasing concentrations of protein and passed over a nitrocellulose filter. The percentage of protein-bound RNA was plotted against protein concentration (see *SI Materials and Methods*). Each binding assay was performed in triplicate; error bars indicate SEM.

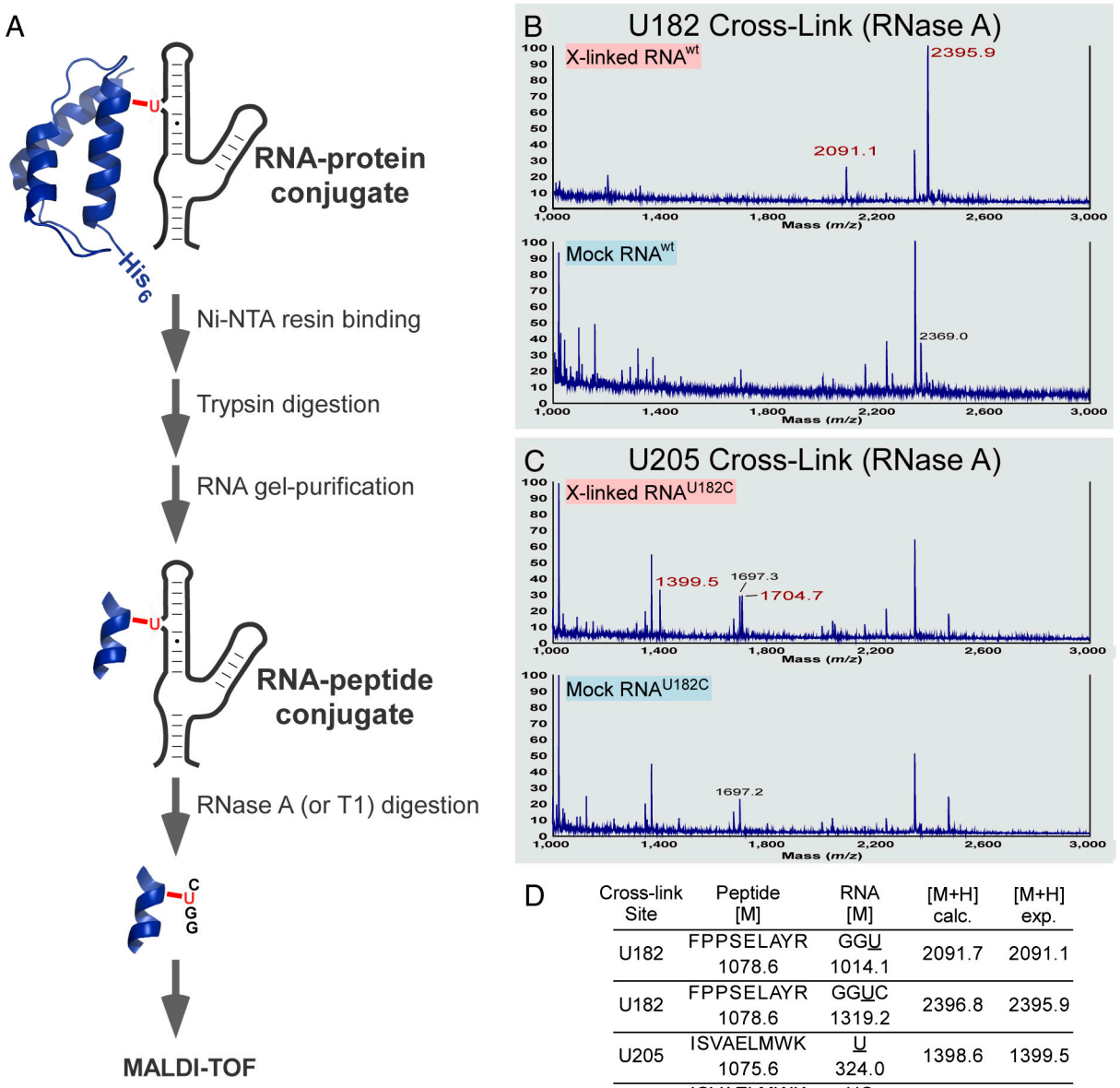

D

Cross-link Site	Peptide [M]	RNA [M]	[M+H] calc.	[M+H] exp.
U182	FPPSELAYR 1078.6	GGU 1014.1	2091.7	2091.1
U182	FPPSELAYR 1078.6	GGUC 1319.2	2396.8	2395.9
U205	ISVAELMWK 1075.6	U 324.0	1398.6	1399.5
U205	ISVAELMWK 1075.6	UC 629.1	1703.7	1704.7
	a	b	=a+b-1	

Fig. S3. Identification of U182 and U205 cross-linked RNA-peptide conjugates. (*A*) Schematic of cross-linked RNA-peptide identification. The cross-linked RNA-peptide conjugates were affinity-purified by Ni-nitrilotriacetate (Ni-NTA) resin under denaturing conditions to remove free RNA. The sample was digested on resin by trypsin and the peptide-linked RNA was purified by denaturing PAGE to remove free peptides. The purified RNA-peptide conjugate was digested by RNase A or T1, and analyzed by MALDI-TOF. (*B*) MALDI-TOF spectrum of RNaseA-treated U182-linked peptides. Two major peaks are observed in the cross-linking sample (X-linked) and not in the non-cross-linking control (Mock) RNA. (*C*) MALDI-TOF spectrum of RNaseA-treated U205-linked peptides. The U182C mutant RNA enriched for the U205-linked RNA-peptide conjugate. (*D*) Expected and observed masses of the RNA-cross-linked peptides. The peptide acquires a single hydrogen during positive-ion MALDI-TOF, resulting in an increased mass of 1 Da.

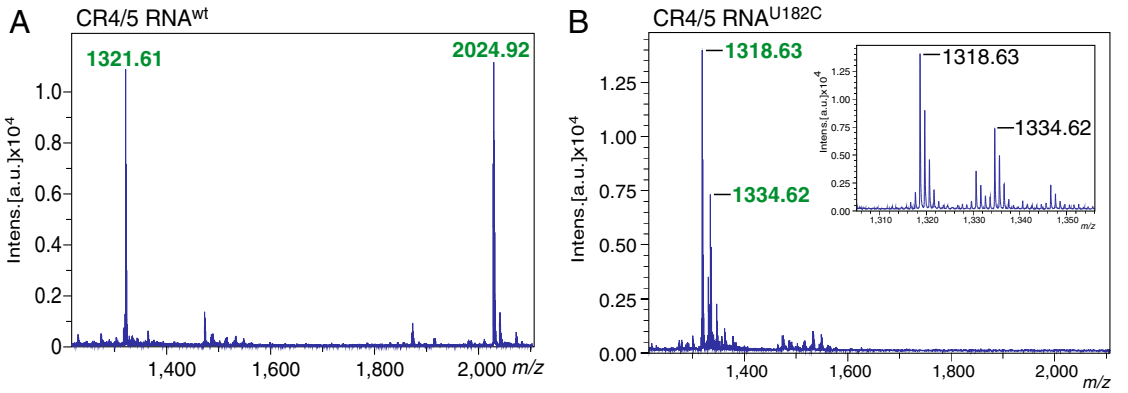

Peptide [M]	RNA [M]	[M+H] calc.	[M+H] exp.
FPPSELAYR 1078.55	U 244.07	1321.62	**1321.61**
LVFFEGLPYLNGQER 1781.91	U 244.07	2024.98	**2024.92**
a	b	=a+b-1	

Peptide [M]	RNA [M]	[M+H] calc.	[M+H] exp.
ISVAELMWK 1075.58	U 244.07	1318.65	**1318.63**
ISVAELMWK 1091.58	U 244.07	1334.65	**1334.62**
a	b	=a+b-1	

Fig. S4. Parent ion selection of uridine-linked peptide for MALDI-TOF/TOF. (*A*) MALDI-TOF analysis of uridine–peptide conjugates. The peak at 1,321.61 Da corresponds to the U182-linked peptide ^{496}FPPSELAYR^{504} and is further analyzed by MALDI-TOF/TOF shown in Fig. 4*A*. The peak at 2,024.92 Da corresponds to the uridine-linked peptide ^{352}LVFFEGLPYLNGQER^{366}. This peptide has a deaminated Asn362 (N) contributing a 1-Da increase in peptide mass (1). (*B*) MALDI-TOF analysis of U205-peptide conjugate. The peak at 1,318.63 Da corresponds to the U205-linked peptide ^{470}ISVAELMWK^{478} and is analyzed by MALDI-TOF/TOF shown in Fig. 4*B*. The second peak at 1,334.62 Da is due to oxidation of Met476 (M) in the same peptide.

1 Tyler-Cross R, Schirch V (1991) Effects of amino acid sequence, buffers, and ionic strength on the rate and mechanism of deamidation of asparagine residues in small peptides. *J Biol Chem* 266:22549–22556.

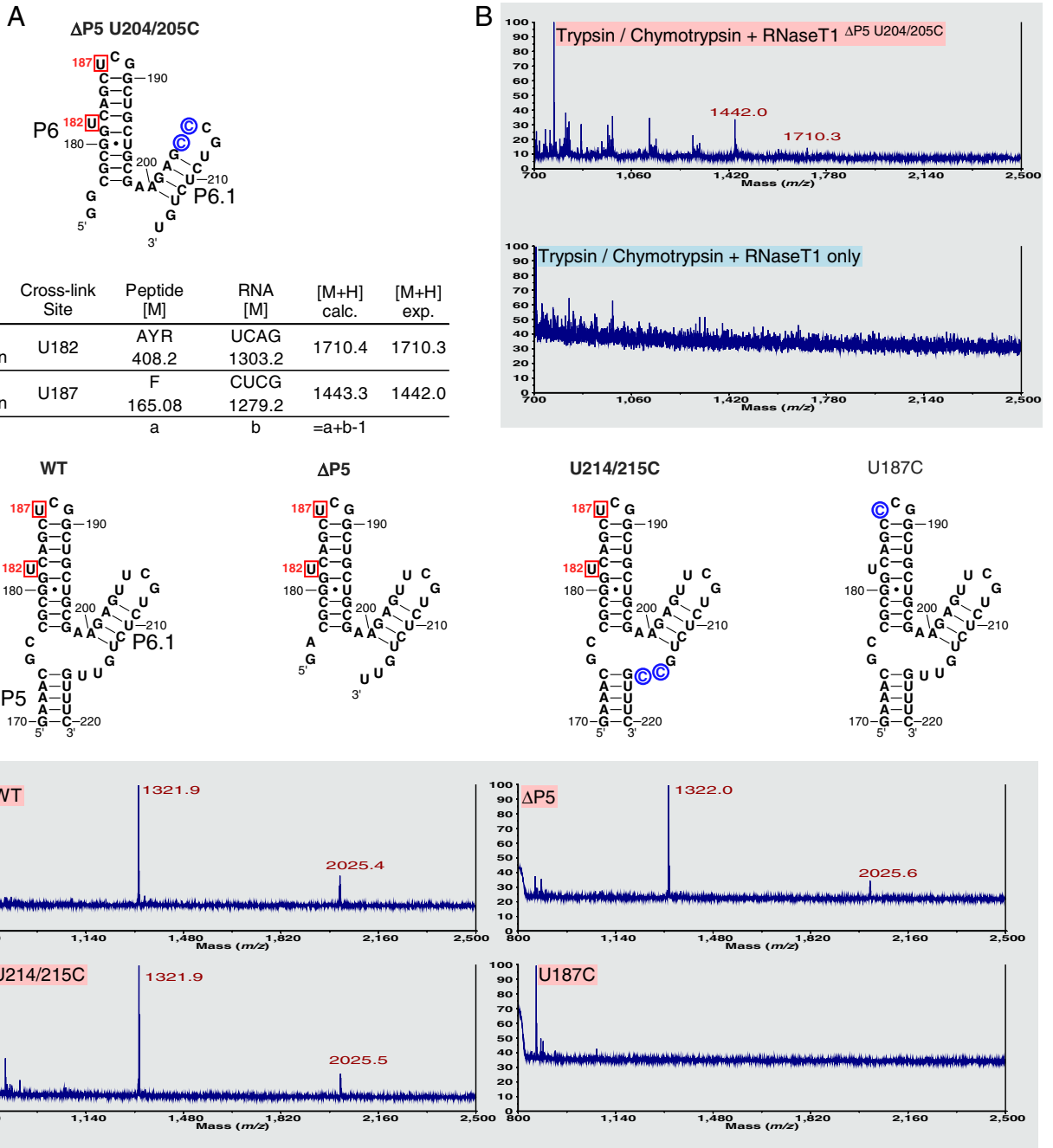

F

Peptide [M]	RNA [M]	[M+H] calc.	[M+H] exp.
FPPSELAYR 1078.5	U 244.1	1321.6	~1321.9
LVFFEGLPYLNGQER 1781.9	U 244.1	2025.0	~2025.5
a	b	=a+b-1	

Fig. S5. Identification of the cross-linking nucleotide U187. (*A*) The secondary structure of CR4/5 RNA used in *B* and *C* with mutations colored blue. (*B*) MALDI-TOF spectrum of U182- and U187-linked peptide conjugates. The CR4/5 RNA mutant with P5 deleted (ΔP5) and U204/205C mutation enriched for the U182 and U187 cross-linked peptides. Trypsin and RNase T1-treated RNA-peptide conjugates were digested with chymotrypsin. Peak at 1,442 Da in trypsin/chymotrypsin double-digested sample (*Upper*) closely matches the expected mass of loop 6 nucleotides cross-linked to a single phenylalanine. This peak is not observed when RNase T1 is digested with both proteases (*Lower*). (*C*) Calculated and experimental masses for U182- and U187-linked RNA-peptide conjugates. (*D*) Secondary structure of ΔP5 U214/215C and U187C RNA mutants. Substituted nucleotides are colored blue. (*E*) MALDI-TOF spectrum of nucleoside-peptide conjugates of CR4/5 mutants. (*F*) Calculated and experimental masses of observed nucleoside-peptide conjugates. U187C mutation eliminates the Phe355 containing nucleoside-peptide (2,025-Da peak).

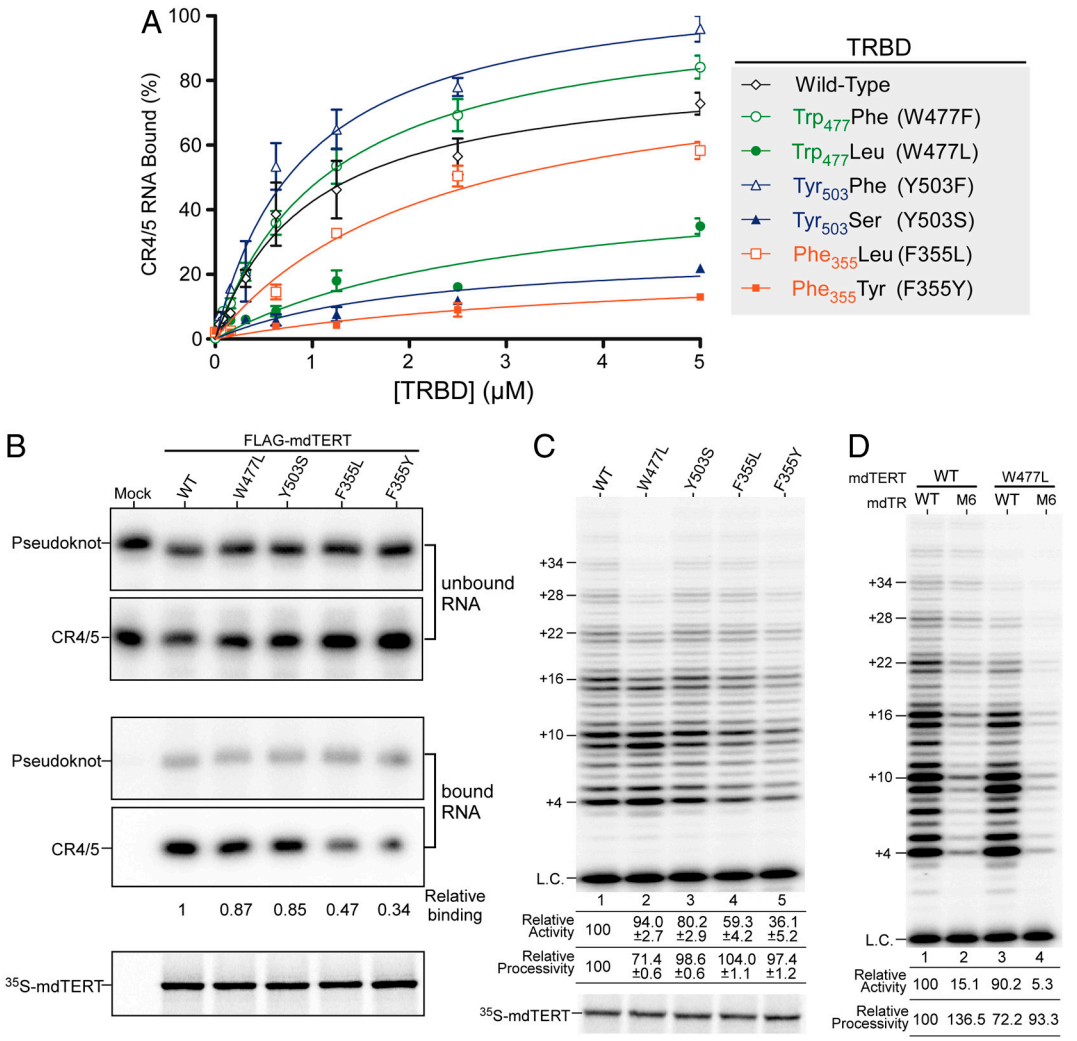

Fig. S6. Effect of TRBD mutations on RNA binding and telomerase activity. (*A*) RNA-binding affinities of purified MBP–TRBD protein mutants. Residues Trp 477, Tyr 503, and Phe355 were mutated to aromatic (Trp477Phe, Tyr503Phe, or Phe355Tyr) or hydrophobic amino acids (Trp477Leu, Tyr503Ser, or Phe355Leu). RNA-binding affinity of the mutant TRBD was measured by filter-binding assay and percent RNA bound was plotted against protein concentration. Assays were performed in triplicate and SEM was indicated. (*B*) Effect of TRBD mutations on full-length TERT protein on RNA binding. Full-length FLAG-tagged medaka TERT proteins were assembled with ^{32}P-labeled CR4/5 and pseudoknot RNA fragments in rabbit reticulocyte lysate (RRL), and immunoprecipitated with anti-FLAG antibody beads. Relative RNA bound was determined by comparing bound to unbound RNA. Relative levels of medaka TERT synthesized in RRL were shown. (*C*) Effect of TRBD mutations on telomerase activity. Full-length medaka TERTs containing TRBD mutations were synthesized in RRL, assembled with medaka TR, and analyzed for telomerase activity using direct primer-extension assay. Relative activity and processivity were quantitated from three separate reactions and standard errors were calculated. L.C. indicates a ^{32}P end-labeled 18-mer DNA loading control. (*D*) Effect of loop L6.1 on telomerase activity and processivity. Wild-type and W477L medaka TERT proteins were assembled with wild-type or L6.1 mutant CR4/5 RNA in RRL, and analyzed for telomerase activity. The L6.1 mutant contains point mutations, U205A and G207C (M6).

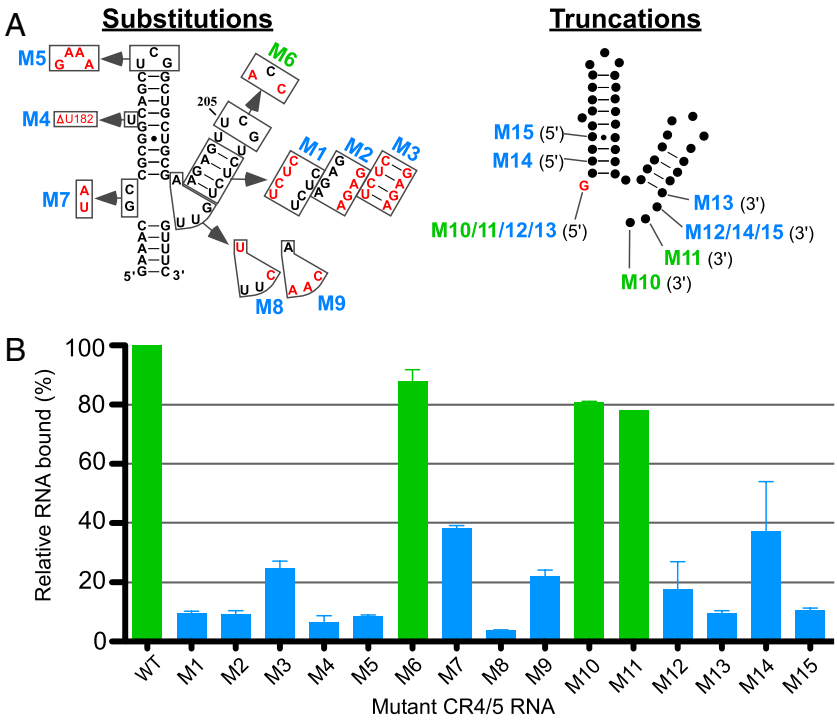

Fig. S7. The minimal CR4/5 domain for TRBD binding. (*A*) Substitution and truncation mutants of CR4/5 RNA. Nucleotides changed in the substitution mutants (*Left*, M1-9) and the 5′/3′ ends of the truncation mutants (*Right*, M10-15) are indicated on the secondary structure. (*B*) TRBD-binding assay of CR4/5 RNA mutants. Percentages of protein-bound RNA (WT and M1-15) were measured using the filter-binding assay with 2.5 μM protein and 5 nM ^{32}P radiolabeled RNA. Percentage of protein-bound over total input RNA is normalized to that of wild-type RNA. Mutant RNAs retaining greater than 75% wild-type RNA TRBD-binding capacity are shown in green, and reduced TRBD-binding capacity less than 40% wild-type RNA TRBD-binding capacity are shown in blue. Error bars indicate SEM.

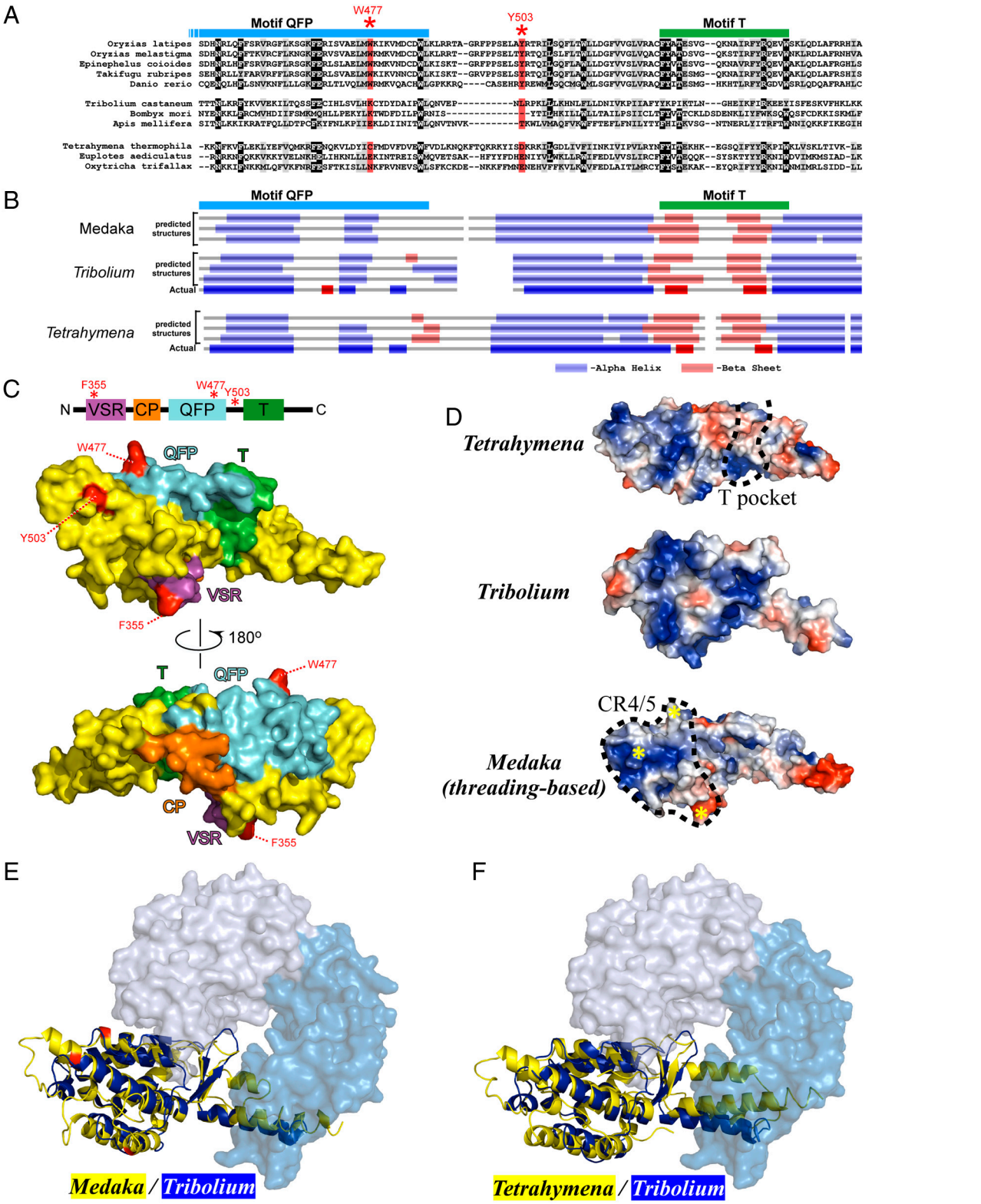

Fig. S8. Mapping cross-linked protein residues on medaka TRBD structural model. (*A*) Multiple sequence alignment of motifs QFP and T. The alignment includes sequences from five fishes, three insects, and three ciliates. Shading indicates identity/similarity greater than 80%. Residues homologous to medaka Trp477 (W477) and Tyr503 (Y503) are shaded in red and indicated by asterisks. (*B*) Secondary structure prediction of motifs QFP and T sequences. Secondary structures were predicted for medaka (*Oryzias latipes*), *Tribolium castaneum*, and *Tetrahymena thermophila* TRBD using algorithms Jpred (1), YASPIN (2), and PSIPred (3). Secondary structures from crystal structures (4, 5) are also shown for *Tribolium and Tetrahymena*. Alpha helices are colored blue and β-sheets are red. (*C*, *Upper*) Organization of TRBD motifs. Four motifs, VSR (violet), CP (orange), QFP (teal), and T (green) are shown. The cross-linked residues are indicated by red asterisks. (*Lower*) Medaka TRBD threading-based model was generated with SWISS-MODEL Workspace (6) using *T. thermophila* TRBD as a scaffold. Motifs and cross-linked residues are colored the same as the above. (*D*) Surface electrostatic charge distribution of TRBD proteins. Positive charges are shown in

blue and negative in red. Previously identified T pocket (5) is shown on the *T. thermophila* structure and CR4/5 binding interface on medaka threading-based homology model. Positions of cross-linked amino acids are indicated by yellow asterisks. (*E*) Superimposition of medaka threading-based TRBD model onto Tribolium TERT structure. The medaka model (yellow) and *Tribolium* structure (blue) were superimposed using DaliLite (7). Cross-linked amino acids are colored red on medaka model. (*F*) Superimposition of *Tetrahymena* TRBD structure onto *Tribolium* TERT structure.

1 Cole C, Barber JD, Barton GJ (2008) The Jpred 3 secondary structure prediction server. *Nucleic Acids Res* 36:W197–201.
2 Lin K, Simossis VA, Taylor WR, Heringa J (2005) A simple and fast secondary structure prediction method using hidden neural networks. *Bioinformatics* 21:152–159.
3 Bryson K, et al. (2005) Protein structure prediction servers at University College London. *Nucleic Acids Res* 33:W36–38.
4 Gillis AJ, Schuller AP, Skordalakes E (2008) Structure of the Tribolium castaneum telomerase catalytic subunit TERT. *Nature* 455:633–637.
5 Rouda S, Skordalakes E (2007) Structure of the RNA-binding domain of telomerase: Implications for RNA recognition and binding. *Structure* 15:1403–1412.
6 Arnold K, Bordoli L, Kopp J, Schwede T (2006) The SWISS-MODEL Workspace: A web-based environment for protein structure homology modelling. *Bioinformatics* 22:195–201.
7 Holm L, Park J (2000) DaliLite workbench for protein structure comparison. *Bioinformatics* 16:566–567.